Structural Evidence for an Octameric Ring Arrangement of SARM1

Michael Sporny [1], Julia Guez-Haddad [1], Mario Lebendiker [2], Valeria Ulisse [3], Allison Volf [1], Carsten Mim [4,5], Michail N. Isupov [6] and Yarden Opatowsky [1]

*1 - **The Mina & Everard Goodman Faculty of Life Sciences,** Bar-Ilan University, Ramat-Gan 5290002, Israel*
*2 - **Wolfson Centre for Applied Structural Biology,** The Hebrew University of Jerusalem, Israel*
*3 - **Department of Biomolecular Sciences,** Weizmann Institute of Science, Rehovot, Israel*
*4 - **Department of Biomedical Engineering and Health Solutions,** Royal Technical Institute (KTH), Stockholm, Sweden*
*5 - **Department of Nutrition and Biosciences,** Karolinska Institute, Huddinge, Sweden*
*6 - **Biosciences,** University of Exeter, England, UK*

***Correspondence to Yarden Opatowsky:** yarden.opatowsky@biu.ac.il*
https://doi.org/10.1016/j.jmb.2019.06.030

Abstract

SARM1 induces axonal degeneration in response to various insults and is therefore considered an attractive drug target for the treatment of neuro-degenerative diseases as well as for brain and spinal cord injuries. SARM1 activity depends on the integrity of the protein's SAM domains, as well as on the enzymatic conversion of NAD+ to ADPR (ADP Ribose) products by the SARM1's TIR domain. Therefore, inhibition of either SAM or TIR functions may constitute an effective therapeutic strategy. However, there is currently no SARM1-directed therapeutic approach available because of an insufficient structural and mechanistic understanding of this protein. In this study, we found that SARM1 assembles into an octameric ring. This arrangement was not described before in other SAM proteins, but is reminiscent of the apoptosome and inflammasome—well-known apoptotic ring-like oligomers. We show that both SARM1 and the isolated tandem SAM$^{1-2}$ domains form octamers in solution, and electron microscopy analysis reveals an octameric ring of SARM1. We determined the crystal structure of SAM$^{1-2}$ and found that it also forms a closed octameric ring in the crystal lattice. The SAM$^{1-2}$ ring interactions are mediated by complementing "lock and key" hydrophobic grooves and inserts and electrostatic charges between the neighboring protomers. We have mutated several interacting SAM$^{1-2}$ interfaces and measured how these mutations affect SARM1 apoptotic activity in cultured cells, and in this way identified critical oligomerization sites that facilitate cell death. These results highlight the importance of oligomerization for SARM1 function and reveal critical epitopes for future targeted drug development.

Introduction

First discovered as a negative regulator of TIR domain-containing adaptor inducing interferon-β (TRIF) in Toll-like receptor signaling [1], sterile α and HEAT/armadillo motif-containing protein (SARM1) was later identified as a predominantly neuronal protein that promotes neuronal death after viral infections [2,3] and oxygen and glucose deprivation [4]. SARM1 is also known to play a key role in Wallerian degeneration [the programmed death of axons following their severing (axotomy) [5] [6]], which is demonstrated by SARM1 suppression in both *Drosophila* [7] and mouse [8] axotomy models that present significantly delayed degeneration.

The domain composition of SARM1 includes an ARM, two SAM, and one TIR domains (Fig. 1A), which are thought to mediate auto-inhibition, oligomerization, and NADase activity, respectively [10]. An N-terminal mitochondria localization peptide guides SARM1 to associate with the outer

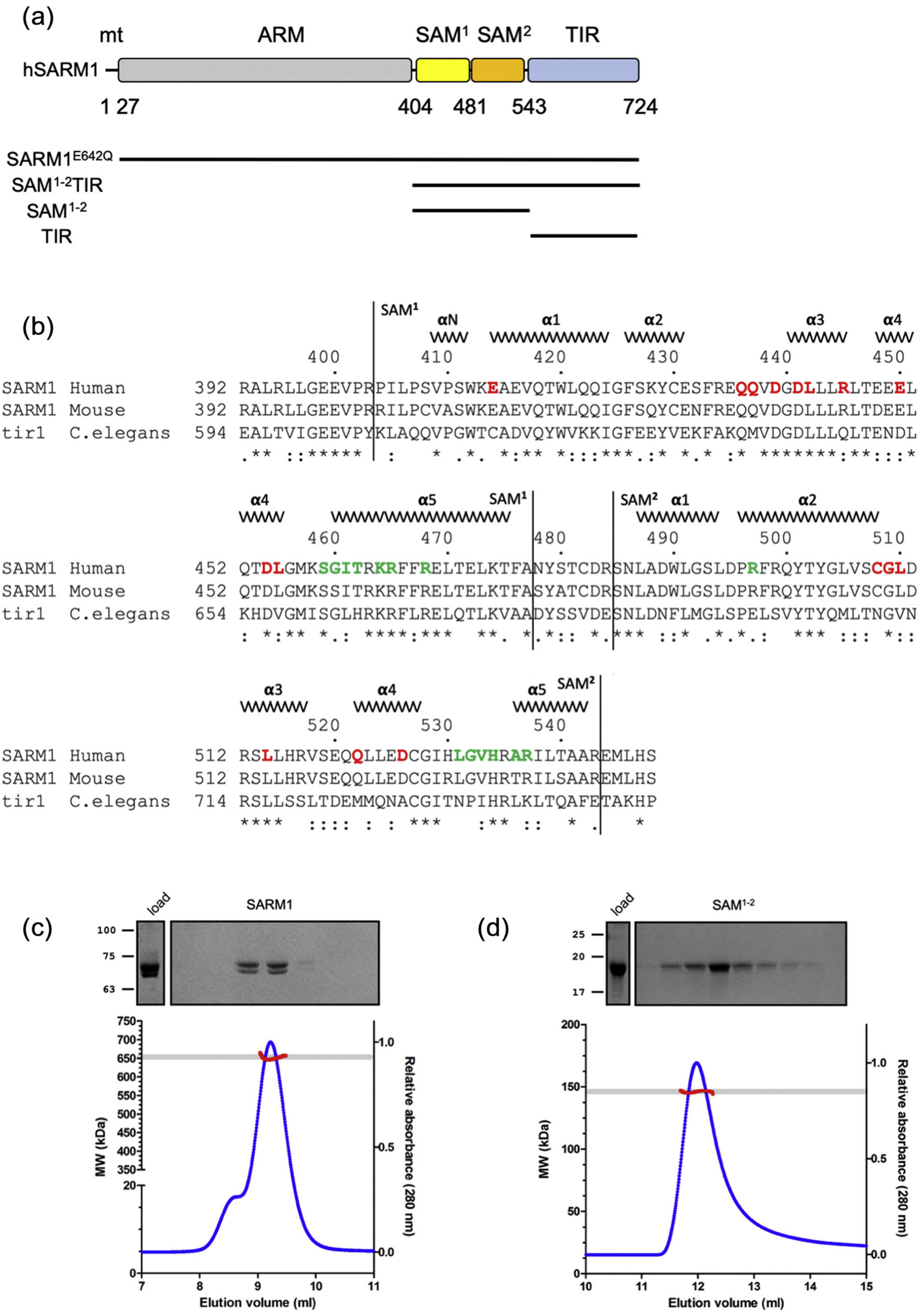
(a)
mt
ARM
SAM¹
SAM²
TIR
hSARM1
1 27
404
481
543
724
SARM1E642Q
SAM1-2TIR
SAM1-2
TIR
(b)
SAM¹
αN
α1
α2
α3
α4
400 410 420 430 440 450
SARM1 Human 392 RALRLLGEEVPRPILPSVPSWKEAEVQTWLQQIGFSKYCESFREQQVDGDLLLRLTEEEL
SARM1 Mouse 392 RALRLLGEEVPRRILPCVASWKEAEVQTWLQQIGFSQYCENFREQQVDGDLLLRLTDEEL
tir1 C.elegans 594 EALTVIGEEVPYKLAQQVPGWTCADVQYWVKKIGFEEYVEKFAKQMVDGDLLLQLTENDL
.** ::***** : * .*. *:** *:::***.:* *.* :* *******:**:::*
α4
α5
SAM¹
SAM²
α1
α2
460 470 480 490 500 510
SARM1 Human 452 QTDLGMKSGITRKRFFRELTELKTFANYSTCDRSNLADWLGSLDPRFRQYTYGLVSCGLD
SARM1 Mouse 452 QTDLGMKSSITRKRFFRELTELKTFASYATCDRSNLADWLGSLDPRFRQYTYGLVSCGLD
tir1 C.elegans 654 KHDVGMISGLHRKRFLRELQTLKVAADYSSVDESNLDNFLMGLSPELSVYTYQMLTNGVN
: *:** *.: ****:*** **. *.*:: *.*** ::* .*.*.: *** ::: *::
α3
α4
α5
SAM²
520 530 540
SARM1 Human 512 RSLLHRVSEQQLLEDCGIHLGVHRARILTAAREMLHS
SARM1 Mouse 512 RSLLHRVSEQQLLEDCGIRLGVHRTRILSAAREMLHS
tir1 C.elegans 714 RSLLSSLTDEMMQNACGITNPIHRLKLTQAFETAKHP
**** :::: : : *** :** :: * . *
(c)
load
SARM1
100
75
63
MW (kDa)
750
700
650
600
550
500
450
400
350
20
0
7 8 9 10 11
Elution volume (ml)
Relative absorbance (280 nm)
1.0
0.5
0.0
(d)
load
SAM1-2
25
20
17
MW (kDa)
200
150
100
50
0
10 11 12 13 14 15
Elution volume (ml)
Relative absorbance (280 nm)
1.0
0.5
0.0

mitochondrial membrane [11], although it is not indispensable in axonal degeneration [8]. It was recently shown that nicotinamide mononucleotide (NMN) can activate SARM1, consistent with its involvement in NAD metabolism [12].

The annotated TIR domain of SARM1 shares low-sequence homology with canonical Toll/interleukin-1 receptors (TIRs) that participate in Toll-related immune responses and mediate protein–protein interactions. Surprisingly, it possesses an enzymatic catalytic activity for nicotinamide adenine dinucleotide (NAD+). In this way, the SARM1 TIR is functionally related to a more distal group of similar-fold enzymes—the nucleoside 2-deoxyribosyltransferase (NDT) family [13] and to certain bacterial TIR-like domains [14]. A single amino acid substitution in the TIR domain (E642A) that abolishes the NADase activity renders SARM1 inactive in axotomy *ex vivo* experiments [13] [15], thereby implicating the role of SARM1 in axonal degeneration with its ability to hydrolyze NAD+. However, ectopic expression of the isolated TIR domain in sarm1$^{-/-}$ DRG explants does not exert degenerative responses [8]; this is likely because the enzymatic TIR activity requires assisted dimerization. TIR superfamily domains homo- and hetero-dimerize with other TIR domains to promote protein–protein interactions [16], and the active site of the structurally related NDT enzymes includes complementation of two interacting domains [17]. Indeed, induced dimerization of SARM1 TIR by fusion protein inserts leads to NAD+ loss and neuronal cell death [18,19]. Similarly, in the absence of the auto-inhibitory ARM domain, SAM–TIR constructs are also active, presumably due to SAM-mediated dimerization [8].

As one of the most abundant protein–protein interaction motifs (there are >200 in the human genome), SAM domains participate in a variety of signal transduction, transcription regulation, and developmental processes [20]. They were first discovered based on sequence homology between 14 different yeast and *Drosophila* proteins [21]. Although all SAM domains share a similar fold, they can actually interact through various molecular surfaces with a wide range of binding partners, including proteins, oligonucleotides, and lipids. Their protein partners can include other domains (e.g., kinases), while some SAM domains homo- and hetero- (with different SAM domains) dimerize [20]. In certain cases, where the binding is mediated through two opposing surfaces designated the mid-loop (ML) and end-helix (EH) motifs, self-association can lead to the formation of an open-end helical polymer [9,22–26]. Previous computational prediction [27] did not identify the SARM1's SAM domains of *Drosophila* and *Caenorhabditis elegans* to form polymers, while an experimental approach [28] indicated oligomerization, but not polymerization, by the human paralog domains.

Facing such a remarkable versatility in binding possibilities [29,30] and due to the very low-sequence homology of the SARM1 SAM domains with other previously characterized SAMs, it is very difficult to predict how they affect SARM1 structure and function.

To learn more about the activation mechanism of SARM1, we have studied the structure and properties of human SARM1. We first observed that SARM1 forms an octamer ring in solution. Next, we determined the 2.5-Å resolution SAM$^{1-2}$ crystal structure that revealed how the unique ring arrangement is facilitated by complementary interacting interfaces from both the SAM^{1} and SAM^{2} domains. The two oligomerization interfaces, as revealed in the crystal structure, are charged and complemented by hydrophobic inserts, the substitution of which results with a diminished capacity for oligomerization. Finally, by conducting assays in cultured cells, we identified the most critical sites for oligomerization that directly affect SARM1 cytotoxic function.

Results and Discussion

SARM1 forms octamers in solution

As multimerization plays a critical role in the enzymatic activity and function of SARM1, we sought to determine the oligomeric state of the protein in solution. To facilitate high-yield production of recombinant protein, suitable for size analysis, we have expressed in mammalian cell culture a form of SARM1 that is truncated at the N-terminal mitochondrial localization peptide (^{26}ERL…GPT^{724}) and mutated in the catalytic E642 residue: SARM1^{E642Q}, and isolated the protein using metal-chelate

Fig. 1. Domain organization and SEC-MALS analysis of hSARM1. (A) Color-coded organization and nomenclature of the SARM1 ARM, SAM, and TIR domains. A mitochondrial localization signal is indicated at the N′ terminal of the protein. The constructs that were used in this study are underlined. (B) Structure-based sequence alignment of human SAM$^{1-2}$ (uniport: Q6SZW1) to the mouse SARM1 (Q6PDS3) and the *C. elegans* homolog tir1 (Q86DA5). The boundaries for the two SAM domains are marked. In each SAM domain, the residues directly involved in mediating inter-molecular interactions are colored in red and green, for the ML and EH surfaces, respectively (see also Figs. 4B and Fig. 5B). (C and D) SEC-MALS analyses reveal octameric arrangement of SARM1 (A) and the SAM$^{1-2}$ domains (B). The elution was analyzed for absorbance at 280 nm (right *y*-axis) and for multiangle light scattering, which was converted to molecular mass (left *y*-axis). SDS-PAGE analyses of SEC-MALS column load and eluate fractions profiles are also presented.

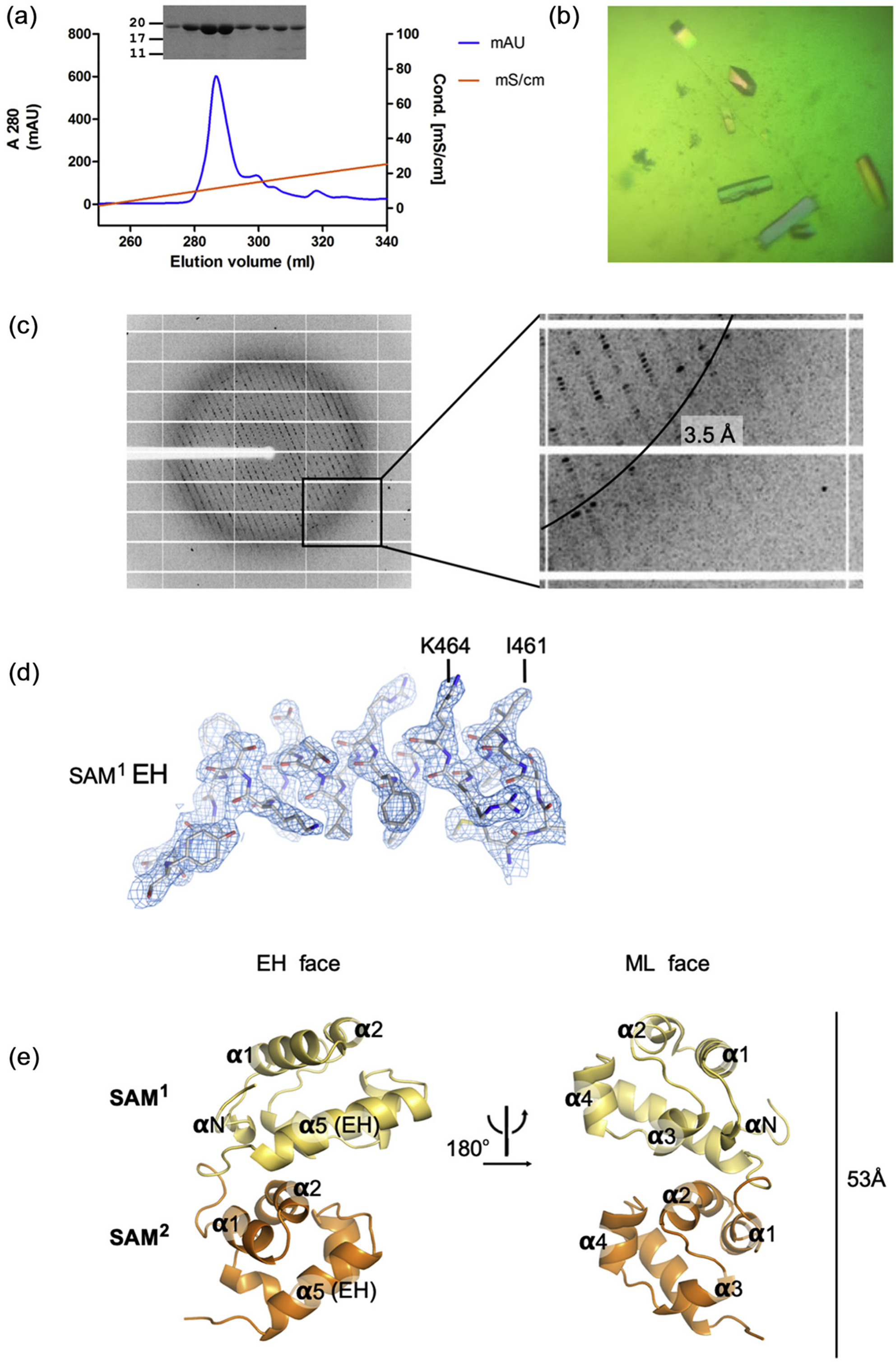
(a)
20
17
11
800
600
400
200
0
A 280 (mAU)
100
80
60
40
20
0
Cond. [mS/cm]
mAU
mS/cm
260
280
300
320
340
Elution volume (ml)
(b)
(c)
3.5 Å
(d)
K464
I461
SAM¹ EH
EH face
ML face
(e)
SAM¹
SAM²
α1
α2
αN
α5 (EH)
α1
α2
α5 (EH)
180°
α2
α1
α4
α3
αN
α2
α1
α4
α3
53Å

chromatography. We next determined the oligomeric order of the protein using size exclusion chromatography with multi-angle light scattering (SEC-MALS) (Fig. 1C). The measured masses by the MALS and RI modules were 5.763×10^5 (±0.011%) and 6.50×10^5 (±0.010%) Da, respectively, accounting for eight SARM1 copies, the predicted weight of which are 6.210×10^5 Da. Assuming that SARM1 oligomerization relies on SAM domains' intermolecular interactions, we also expressed and purified SAM$^{1-2}$. Initially, we based the construct design on the predicted SAM domains' boundaries (^{412}WKE… LHS^{548}). However, this construct proved to be insoluble at high concentration. We then considered that inclusion of flanking segments may be useful and included a 20-residue amino-extension (^{392}RAL…LHS^{548}, Fig. 1B), which indeed improved solubility dramatically. Native SAM$^{1-2}$ was expressed as a NusA fusion in *Escherichia coli* and purified (Fig. 1D and 2A). With a predicted octameric mass of 1.492×10^5, SEC-MALS analysis of SAM$^{1-2}$ (Fig. 1D) clearly demonstrates octameric arrangement, with a measured MALS and RI masses of 1.381×10^5 (±0.033%) and 1.456×10^5 (±0.033%) Da, respectively.

Crystallography

To obtain high-resolution data about SARM1 oligomerization, we pursued the crystallization of the SAM$^{1-2}$ domains. Screening for crystallization conditions using the commercial crystallization screens produced many (>20) hits. After refinement of the crystallization conditions, best diffracting crystals were grown from 2% Tacsimate (pH 7), 5% v/v 2-propanol, 0.1 M imidazole (pH 7), and 8% w/v polyethylene glycol 3350 (Fig. 2B). Crystals were gradually introduced to a cryo-protectant solution consisting of 15% glycerol that was added to the mother-liquor and flash-frozen in liquid N_2.

The native crystals belonging to the $P4_3$ space group, with unit cell dimensions of $a = b = 252.3$, $c = 49.8$, $\alpha = \beta = \gamma = 90°$ contain 16 molecules in the asymmetric unit and have a solvent content of 55%. The crystals diffracted to a maximal resolution of 2.47 Å (Fig. 2C). Molecular replacement was ineffective in our attempts to solve the structure; this was most likely due to the low homology to other SAM domains that have available structures, as well as the high copy number (16 SAM$^{1-2}$, with a total of 32 individual SAMs) in the asymmetric unit. Eventually, we produced selenomethionine derivative crystals and collected SeMet peak data sets to solve the crystal structure using the single-wavelength anomalous dispersion (SAD) method in the Crank2 experimental phasing pipeline (Table 1) [31]. SAD phasing was followed by NCS averaging, model building, electron density modification procedures, and cycles of model refinement and re-building. Except for the 10 N-terminal residues (^{392}RAL… EEV^{401}) of SAM^1, the electron densities of all other residues were modeled into the electron density (Fig. 2D). The final model was refined to 2.47-Å resolution to an *R* factor/*R* free of 18.9%/23.0%.

Overall crystal structure of SAM$^{1-2}$

The crystal structure (Fig. 2E), 53 Å in length, shows that both the SAM^1 and SAM^2 domains of SARM1 have a canonical SAM fold, each with five helices, designated α 1–5. SAM^1 contains an additional N-terminal short helix that packs against a hydrophobic surface generated by helices α 3 and 5. The structural similarity between these domains is high, where 54 Cα atoms (out of a span of 61 core residues) of SAM^1 and SAM^2 superimpose with an RMS deviation of 1.75 Å. The two domains directly interact with each other, mainly through helices α 3 and 5 of SAM^1 and helix α2 of SAM^2, and are related by a near-perfect head-to-tail longitudinal translation.

SAM$^{1-2}$ crystal-contact analysis

The asymmetric unit includes two virtually identical rings, each formed by eight laterally packed SAM$^{1-2}$ molecules, with outer and inner ring diameters of 97 and 36 Å, respectively (Fig. 3A). SAM^1 and SAM^2 have similar electrostatic potential and hydrophobic surface distributions (Fig. 3B), with an electronegative ML face and a complementary electropositive EH face. In addition, on the tip of the EH helices (i.e., α 5), hydrophobic side-chains—I^{461} of SAM^1 and V^{533} of SAM^2—insert into complementary hydrophobic clefts at the centers of the reciprocal ML surfaces. In this way, electrostatic attraction draws the neighboring SAM$^{1-2}$ molecules together through a steering effect [32], while the hydrophobic interactions coordinate their positions as “lock-and-key”

Fig. 2. X-ray crystallography of SAM$^{1-2}$. (A) SAM$^{1-2}$ anion-exchange chromatography, using monoQ 10/100 GL (GE Healthcare), salt gradient elution profile chromatogram, and corresponding SDS-PAGE analysis. (B) Crystals of SAM$^{1-2}$ grown in 2% Tacsimate (pH 7), 5% v/v 2-propanol, 0.1 M imidazole (pH 7), and 8% w/v polyethylene glycol 3350. Single crystal dimensions were approximately 0.05 × 0.05 × 0.1 mm. (C) A diffraction image collected at ID29 ESRF using a PILATUS 6 M detector, recorded during data set collection. (D) A refined 2Fo-Fc electron density map contoured to 1.8σ and focusing on the α 5 helix (EH) of the SAM^1 domain. Indicated are the key residues I461 and K464. (E) Crystal structure of the SAM$^{1-2}$ monomer. The structure of SAM$^{1-2}$ displayed as a cartoon, showing the ML and EH faces. SAM^1 is colored in yellow and SAM^1 in orange. Individual helixes are indicated.

Table 1. Summary of crystallographic statistics.

Crystal	Native	Se-Met
Beamline	ID23 ESRF	BL14.2 BESSY
Wavelength (Å)	0.9795	0.9794 (peak)
Space group	$P4_3$	$P4_3$
Unit cell parameters (Å)	$a = b = 252.2$, $c = 49.8$, $\alpha = \beta = \gamma = 90°$	$a = b = 252.8$, $c = 49.8$, $\alpha = \beta = \gamma = 90°$
Total reflections[a]	511,382 (25,603)	622,999 (31,348)
Unique reflections[a]	113,145 (5572)	92,757 (4493)
Completeness (%)[a]	99.4 (99.9)	99.8 (100.0)
Multiplicity[a]	4.5 (4.6)	6.7 (7.0)
R_{meas} (%)[a,b]	14.9 (226.5)	17.4 (168.2)
R_{pim}[a,b]	6.8 (103.1)	6.7 (63.3)
$\langle I \rangle / \langle \sigma(I) \rangle$[a]	7.8 (0.8)	9.3 (1.3)
Resolution range (Å)[a]	56.40–2.47 (2.51–2.47)	89.38–2.65 (2.70–2.65)
$CC_{1/2}$[a,c]	0.994 (0.300)	0.997 (0.455)
Wilson *B*-factor[d] (Å^2)	65.4	65.6
Phasing statistics		
No. of scatterers (ordered)	–	32 (24)
FOM (after density modification)	–	0.177 (0.483)
Refinement statistics		
R_{work}	0.189	–
R_{free}	0.230	–
No. of protein monomers in a.u.	16	16
Number of atoms	20,213	–
Macromolecules	19,051	–
Solvent	1162	–
Protein residues	2337	–
RMS bond lengths (Å)	0.007	–
RMS bond angles (°)	1.46	–
Ramachandran favored (%)	98.2	–
Ramachandran outliers (%)	0.09	–
Clashscore	4.40	–
Average *B*-factor (Å^2)	58.2	–
RCBS PDB code	6QWV	–

[a] Values for the highest-resolution shell are given in parentheses.

[b] $R_{\mathrm{pim}} = \Sigma_h[m/(m-1)]^{1/2}\Sigma_i| I_{h,i} - \langle I_h \rangle |/\Sigma_h\Sigma_i I_{h,i}$; $R_{\mathrm{meas}} = \Sigma_h[1/(m-1)]^{1/2}\Sigma_i| I_{h,i} - \langle I_h \rangle|/\Sigma_h\Sigma_i I_{h,I}$.

[c] $CC_{1/2}$ is defined in [58].

[d] Wilson *B*-factor was estimated by SFCHECK [59].

inserts. The tandem SAM^1–SAM^1 and SAM^2–SAM^2 lateral interactions not only provides stronger binding but also explain the unusual closed ring arrangement. In other cases, where single SAM domains are involved in lateral EH to ML interactions, a helical polymer is formed (Fig. 4A) [9,22–26]. This happens because of the small size of the SAM domain and the angular flexibility of the EH-ML interface. Unlike these proteins, the tandem lateral interactions of the SARM1 SAM$^{1–2}$ domains (Fig. 4B) with 800-Å^2 buried surface area impose rigidity that restricts the oligomerized molecules to a fixed plain and closed oligomer, which prevents polymer spiral organization.

Electron microscopy

After demonstrating by SEC-MALS that SARM1 is an octamer in solution, we considered whether, like the isolated SAM$^{1–2}$ domains, SARM1 forms an octameric ring assembly.

To see if this is the case, we pursued electron microscopy analysis, for which purified SARM1 was first placed on thin carbon films. These films were subsequently stained with a uranyl acetate solution, followed by EM visualization (Fig. 5A), classification, and 2D class averaging (Fig. 5B) of >12,000 negatively stained SARM1 particles. The EM analysis reveals an 8-fold symmetry ring-like structure with one inner ring that is spaced apart from a larger peripheral ring. The peripheral ring includes two distinct types of densities, each having eight copies (Fig. 5C). The 8-mer SAM$^{1–2}$ crystal structure superimposes exactly to the inner ring of the prevalent class average (Fig. 5D), leaving the outward ring densities to the ARM and TIR domains.

Probing the SAM$^{1–2}$ oligomerization interface

It was previously shown, using pull-down experiments of co-expressed SARM1 constructs [8], that the SAM$^{1–2}$ domains facilitate SARM1 homo-intermolecular interactions, and that by removing the SAM domains, SARM1 loses its pro-degenerative function in damaged neurons. Here,

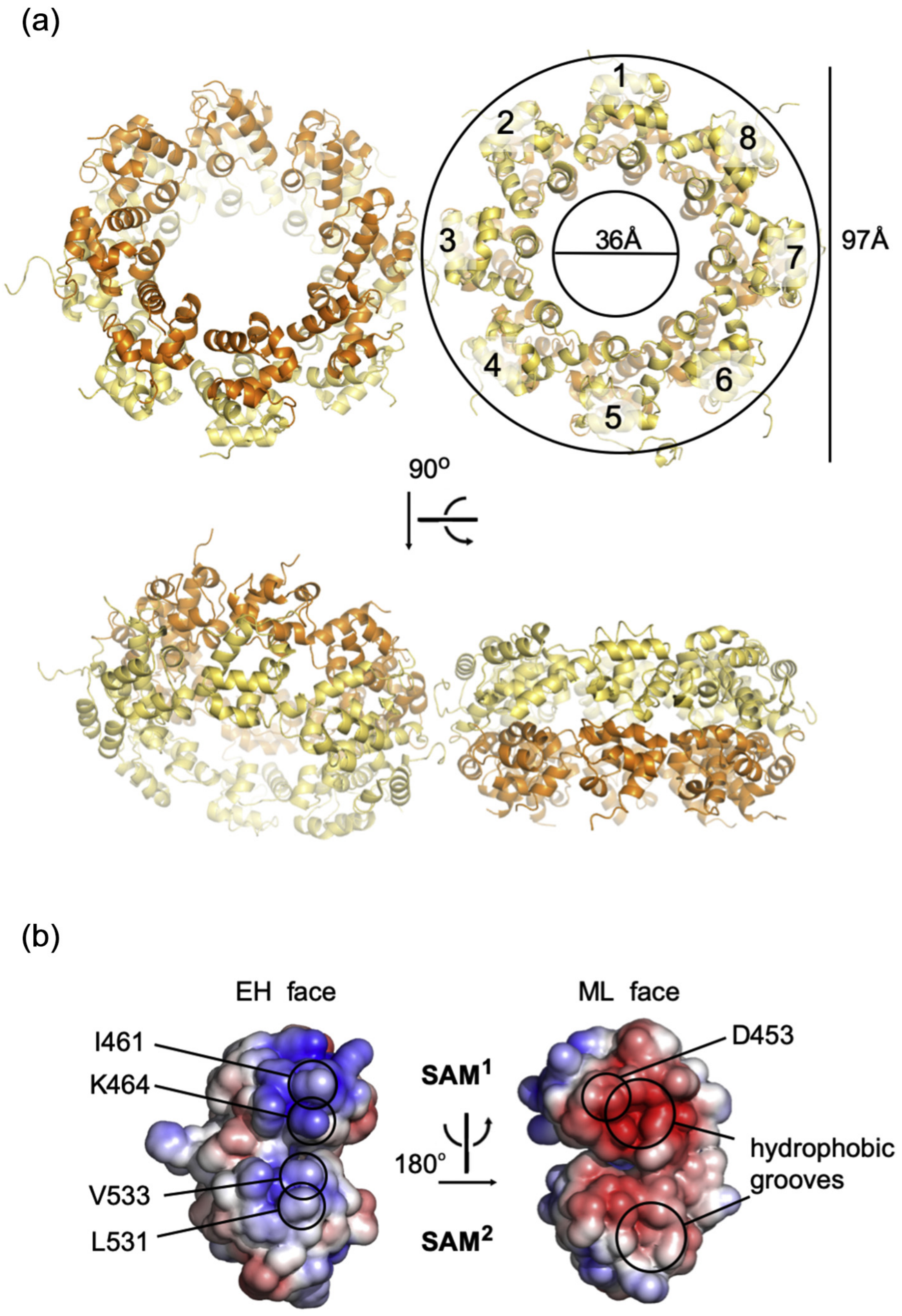

Fig. 3. Inter-molecular interactions in the crystallographic asymmetric unit. (A) The asymmetric unit contains 16 non-crystallographically related SAM$^{1-2}$ protomers arranged in two non-parallel, yet virtually identical rings. Each ring includes eight SAM$^{1-2}$ protomers, packed by lateral head-to-head (SAM^{1}–SAM^{1}) and tail-to-tail (SAM^{2}–SAM^{2}) interactions. (B) Complementarity in electrostatic potential in the SAM$^{1-2}$ oligomeric interface. The right panel shows a view following a rotation of 180° along the vertical axis of the electrostatic surface presented in the left panel, as in Fig. 2E. The electrostatic surface potential is colored in blue (positive) and red (negative).

we set to investigate whether the SAM domains directly affect SARM1 activity by virtue of the intermolecular interactions that they mediate. First, we subjected purified native SAM$^{1-2}$ to chemical cross-linking and SDS-PAGE analysis (Fig. 6A). Distinctive dimeric species soon appeared along with several higher molecular weight bands that are more difficult to distinguish. Next, with the SAM$^{1-2}$ crystal structure in hand (Fig. 3B), we introduced several amino acid substitutions on the EH and ML

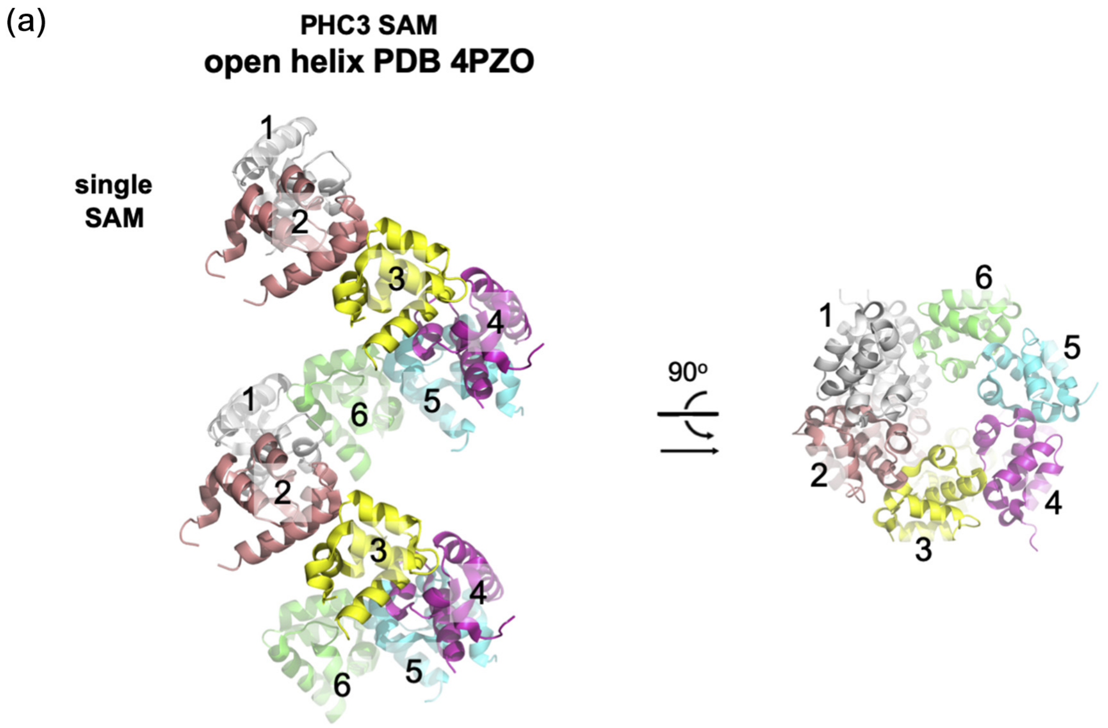

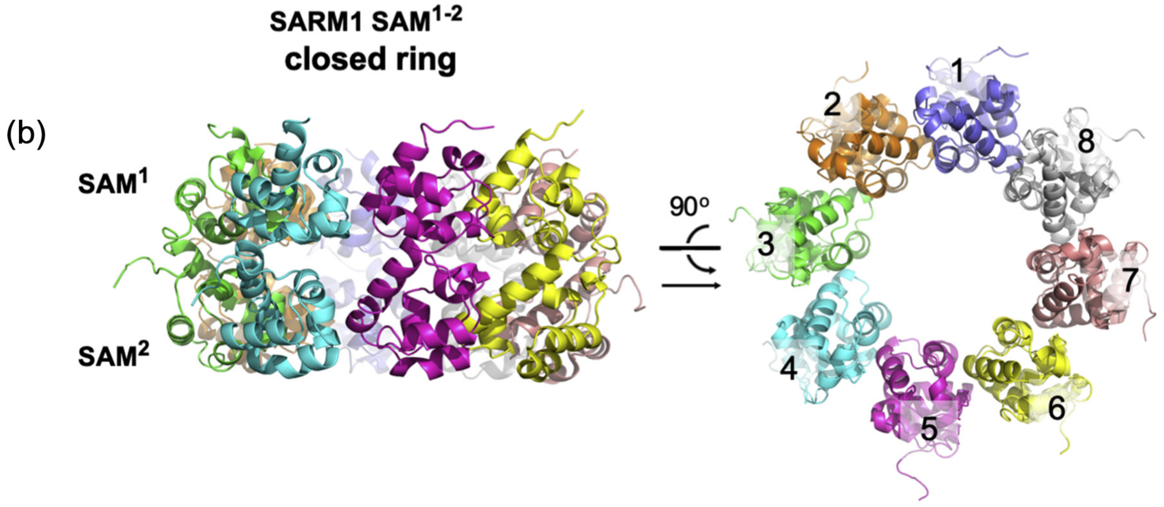

Fig. 4. SAM domain oligomerization: open-end helix *versus* closed ring. (A) A previously determined crystal structure (PDB 4PZO) [9] shows an open-end helix homo-oligomer (top), assembled through interactions between the ML and EH molecular surfaces of neighboring SAM domains. (B) In the SARM1 crystal structure (bottom), the inter-molecular interactions also involve the ML and EH molecular surfaces, but unlike the single SAM homo-oligomer that is more flexible, the tandem arrangement of the SAM$^{1-2}$ imposes spatial constrains that yield a planar, closed ring.

motifs of the SAM^1 and SAM^2 domains, designed to interfere with intermolecular contacts, but without compromising the protein's structural integrity. The various SAM$^{1-2}$ mutants (D454K, I461D, K464D, I461D/K464D, L531D/V533D) were expressed and purified in the same way as the native protein and were subjected to the same chemical cross-linking treatment. Interestingly, SAM^1 mutations (D454K, I461D, K464D) were more effective in compromising homo-intermolecular interactions than the mutations targeting SAM^2 (L531D, V533D) (Fig. 6A), which suggests that the SAM^1–SAM^1 contacts have a more dominant contribution than SAM^2–SAM^2 in SARM1 oligomerization.

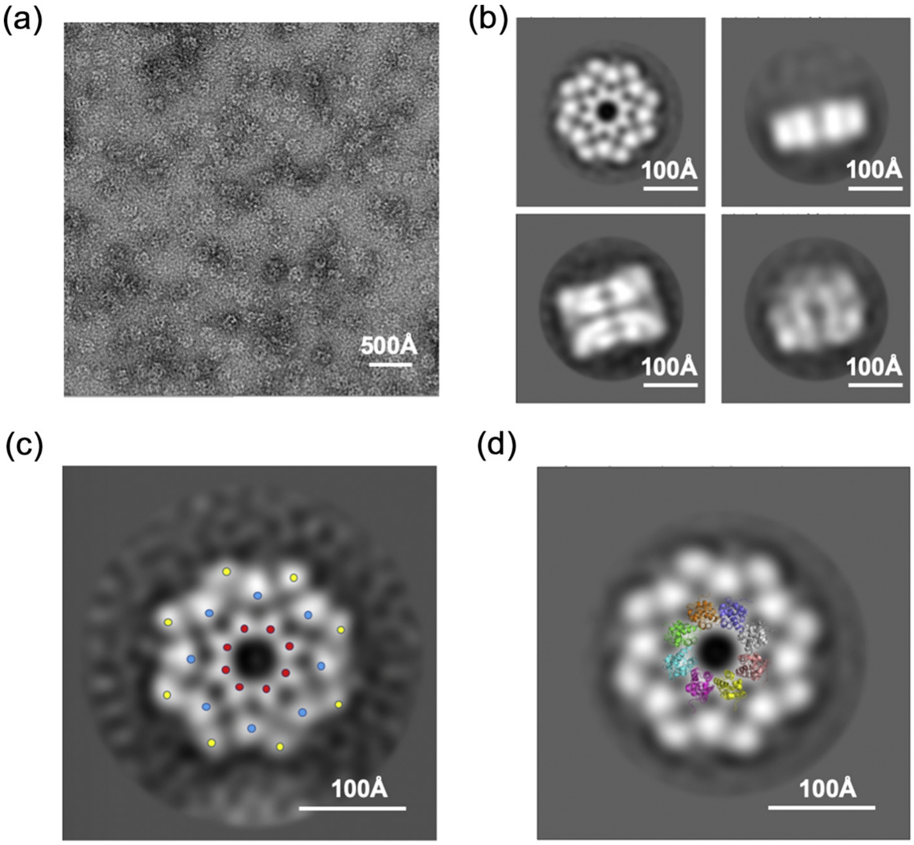

Fig. 5. Octameric ring arrangement revealed by electron microscopy analysis of SARM1. (A) EM micrograph of individual SARM1 particles attached to glow-discharged carbon film stained with 1% uranyl acetate and imaged with a JEOL 2100f electron microscope operating at 200 kV, using a 4k pixel CCD camera (TVIPS, Germany) at a pixel size of 1.75 Å. (B) Four representative 2D class averages after reference-free alignment and classification. Most particles (>60%) show views consistent with preferential attachment of SARM1 particles to the carbon film via the wide face ring octamer, perpendicular to the central cavity (up left). Other classes represent a tilted view of the ring octamer (10% of particles; right up and bottom), and one average represents a class of particles in which two rings are attached together (6% of particles; bottom left). (C) Eight-fold symmetry is observed in three distinct densities in the prevalent class average; these are marked by red, blue, and yellow dots. (D) The SAM$^{1-2}$ octamer crystal structure superimposes well to the inner ring of the prevalent class average, indicating that the periphery ring densities account for the ARM and TIR domains.

Linking SAM$^{1-2}$ oligomerization and SARM1-mediated cell degeneration

It was previously shown that ectopic expression of SAM$^{1-2}$–TIR (res. 409–724) is toxic in neurons and HEK293 cells [8], presumably due to the removal of auto-inhibitory constraints imposed by the ARM domain. It was also shown that the isolated TIR domain (res. 561–724) does not lead to cell death. Here, in order to evaluate the influence of SAM oligomerization on SARM1-mediated cell degeneration, several SAM$^{1-2}$–TIR constructs (Fig. 1A) and mutants were transiently expressed in HEK-293T cells and the effect on cells viability was monitored using the resazurin fluorescence assay (Fig. 6B), in a similar way to that previously demonstrated [8,14]. We have introduced the same set of mutations that were tested in the chemical cross-linking experiments (D454K, I461D, K464D, I461D/K464D, L531D/V533D) to the SAM$^{1-2}$–TIR mammalian expression vector. The results (Fig. 6B) show a perfect correlation between the level of oligomerization, as reflected in the SAM$^{1-2}$ cross-linking experiment with toxicity levels in HEK293T cells. In this way, the mutations that are most effective in inhibiting cytotoxicity are those showing the lowest oligomerization levels, while the most toxic constructs—also form the strongest oligomers. Clearly, SAM^2 mutations (L531D/V533D) are significantly less effective than those mapped to the oligomerization sites of SAM^1, consistent with the poor impact that these mutations had over oligomerization. When introduced separately, the SAM^1 EH mutations I461D and K464D each had a moderate effect, but

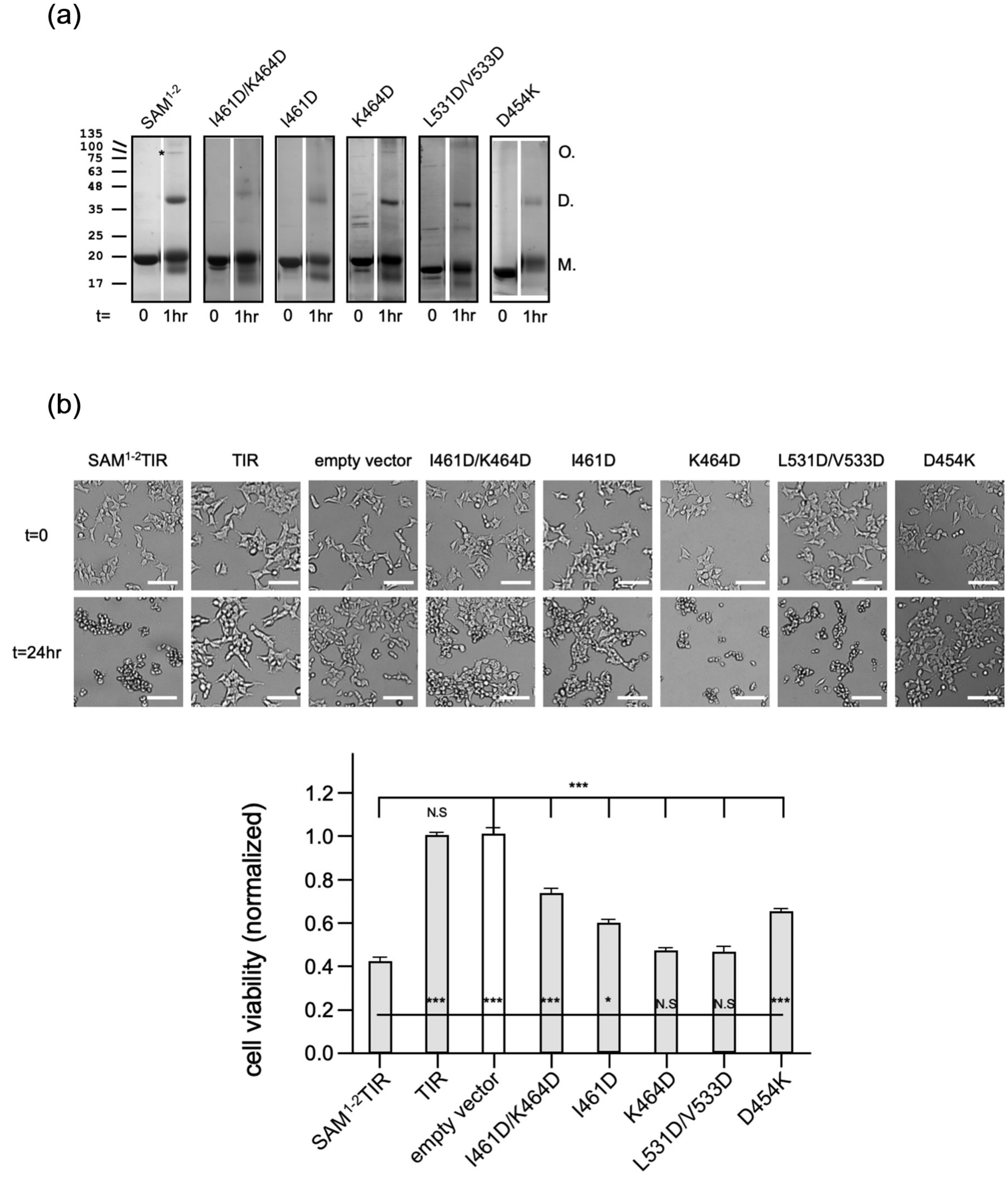

Fig. 6. Linking SARM1 oligomerization and function. (A) SDS-PAGE analysis of SAM$^{1-2}$ and mutants 1 h after cross-linking by glutaraldehyde was commenced. In the native SAM$^{1-2}$, besides the monomer (M.) band, a prominent dimer (D.) and a minor oligomer (O.) bands (marked by an asterisk) are visible. SAM$^{1-2}$ mutants show less dimers and, with the exception of K464D, no oligomers. (B) Toxicity of the SAM$^{1-2}$–TIR construct and mutants in HEK293T cells. Top: representative images of cultured HEK293T cells right after (upper panel) and 24 h post-transfection (lower panel). The cells were transfected with SARM1 constructs' expression vectors and control, as indicated. The scale bar represents 100 μm. Bottom: cell viability was measured and quantification 24 h post-transfection using the fluorescent resazurin assay. While cell viability is virtually unaffected by ectopic expression of the isolated TIR domain, inclusion of the oligomerizing SAM$^{1-2}$ domains (the SAM$^{1-2}$–TIR construct) induces massive cell death, when compared to empty vector (three biological repeats, Student *t* test; $*** p < 0.001$; $* p < 0.05$; n.s: no significance). Mutations at the oligomerization interface affect cell death correlatively as they interfere with SAM$^{1-2}$ oligomerization (as seen in panel A).

when introduced together (I461D/K464D) showed an accumulative response. Remarkably, as shown by Gerdts *et al.* [8], expression of the TIR domain alone (res. 559–724) has no effect over HEK293T viability and is entirely dependent on SAM fusion to reach measurable cytotoxic levels, which highlights the importance of accurate spatial positioning of the TIR domain for SARM1 activity.

Conclusions

Both the elongation of neuronal axons and their elimination are equally important processes in the development and plasticity of the nervous system. Nevertheless, it is considered that inhibition of axon degeneration would prove beneficial in the treatment of certain neurodegenerative disorders, spinal cord injury, and stroke. As the protein SARM1 shows pro-degenerative neuronal activities, strategies for SARM1 inhibition are under pursuit.

In this report, we focused on studying the structure and oligomeric arrangement of human SARM1. Our main focus was the tandem SAM domains of human SARM1, domains that were previously shown to mediate SARM1 oligomerization and are required for its activity. The crystal structure of SAM$^{1-2}$ reveals a unique oligomerization arrangement of a closed octameric ring, consistent with the SEC-MALS and EM analyses of SARM1. Complemented by cell assay experiments, the new crystal structure we obtained provided the molecular underpinnings necessary to design point mutation that effectively inhibited SARM1 degenerative activity without compromising the structural integrity of the protein.

Important questions remain to be addressed; for example, in what way does the ARM domain impose auto-inhibition, and how does nicotinamide mononucleotide leads to SARM1 activation at the molecular level? And the most fascinating question: Is there a particular functional relevance for the octameric ring arrangement of SARM1, considering its resemblance to other degenerative complexes, that is, apoptosome and inflammasome [33], and in light of the recently discovered interplay between SARM1 and the inflamosome [34]?

Experimental Procedures

cDNA generation and subcloning

Cloning of all the constructs was made by PCR amplification from the complete cDNA clone (Imagene) of human SARM1 (uniport: Q6SZW1). Two different SAM$^{1-2}$ constructs (^{412}WKE…LHS^{548} and ^{387}SAL…LHS^{548}) were ligated into a modified pET43 plasmid containing N terminal NusA and His tags, followed by a TEV digestion sequence. For expression in mammalian cell culture and resazurin cell viability assay, SARM1^{E642Q} (^{26}ERL…GPT^{724}), WT and mutated (D454K, I461D, K464D, I461D/K464D, L531D/V533D) SAM–TIR (^{387}SAL…GPT-^{724}), and TIR alone (^{559}GDT…GPT^{724}) constructs were ligated into a modified pEGFP-N1 mammalian expression plasmid missing the C-terminus GFP fusion protein, which includes N-terminal 6*HIS-Tag followed by a TEV digestion sequence. Assembly PCR mutagenesis (based on https://openwetware.org/wiki/Assembly_pcr) was used to introduce all the point mutations.

Protein expression and purification

For bacterial expression, all the constructs were expressed in the T7 Express *E. coli* strain (NEB), also containing the RIL Codon Plus plasmid.

For native SAM$^{1-2}$ proteins, transformed *E. coli* cells were grown for 3–4 h at 37 °C in 2xYT media containing 100 μg/mL ampicillin and 34 μg/mL chloramphenicol. When the culture has reached OD_{600} = 0.6, protein expression was induced with 200 μM IPTG over a 16-h period at 16 °C. For selenomethionine-substituted SAM$^{1-2}$ expression, we followed the same protocol as in Ref. [35], where a newly transformed single *E. coli* colony was grown overnight at 37 °C in 10% LB medium and 90% New Minimal Medium (NMM: 22 mM KH_2PO_4, 50 mM K_2HPO_4, 7.5 mM ammonium sulfate, 8.5 mM NaCl, 1 mM $MgSO_4$) containing 100 μg/mL ampicillin and 34 μg/mL chloramphenicol. After overnight growth, the LB-NMM medium was removed by centrifugation and cells were resuspended in pre-warmed NMM [with addition of 7.2 g glucose, 50 mg of all amino acids except methionine and enriched with 5 mL Kao and Michayluk vitamin solution (Sigma) per liter]. After the culture reached OD_{600} = 0.35–0.4, the temperature was reduced to 16 °C and lysine, phenylalanine and threonine (100 mg/L), isoleucine, leucine and valine (50 mg/L), and DL-selenomethionine (50 mg/L) were added. When the culture growth reached OD_{600} = 0.6, protein expression was induced with 200 μM IPTG over a 16-h period. Cells were harvested and frozen prior to lysis and centrifugation. Both native (WT and mutants) and SeMet SAM$^{1-2}$ were purified in the same way as in Ref. [36]: cells were suspended at a 1:10 (w:v) ratio with lysis buffer [50 mM Tris buffer (pH 7.5), 300 mM NaCl, 10% glycerol, 5 mM β-mercaptoethanol (βME), 0.1% Triton] and lysed using a microfluidizer (Microfluidics). The cell debris was removed by 20-min centrifugation (10,000*g*) at 4 °C, and supernatant was then loaded onto a pre-equilibrated Ni-chelate column (HisTrap, GE Healthcare) with binding buffer [50 mM Tris buffer (pH 7.5), 300 mM NaCl, 5% glycerol, 5 mM βME]; next, it was washed and eluted against an elution buffer gradient [50 mM

Tris (pH 7.5), 300 mM NaCl, 5% glycerol, 500 mM imidazole, 5 mM βME]. Protein-containing fractions were incubated at 4 °C with TEV protease (1:50 w/w) overnight under constant centrifugation (3200*g*) to prevent massive precipitation. The protein was then diluted (1:10) with 25 mM Hepes (pH 7.5), 5% (v:v) glycerol, and 1 mM DTT, loaded on an anion exchange monoQ column (GE Healthcare) and eluted with gradient of 25 mM Hepes (pH 7.5), 5% (v:v) glycerol, 1 mM DTT, and 1 M NaCl. Protein containing fractions were pooled, concentrated, split into aliquots, flash-frozen in liquid N_2, and stored at −80 °C.

SARM1^{E642Q} was expressed in HEK293F suspension cell culture, grown in FreeStyle™ 293 medium (GIBCO), at 37 °C and in 8% CO_2. Transfection was carried out using preheated (70 °C) 40 kDa polyethylenimine (PEI-MAX) (Polysciences) at 1 mg of plasmid DNA per 1 L of culture once cell density has reached 1×10^6 cells/mL.

Cells were harvested 5 days after transfection by centrifugation (10 min, 1500*g*, 4 °C), resuspended with buffer A [50 mM phosphate buffer (pH 8), 400 mM NaCl,5% glycerol, 5 mM BME] and lysed using a microfluidizer followed by two cycles of centrifugation (12,000*g* 20 min). Supernatant was than filtered with 45-μm filter and loaded onto a pre-equilibrated Ni-chelate column. The column was washed with buffer A until a stable baseline was achieved. After applying a 70–200 mM imidazole gradient elution, protein-containing fractions were selected and pooled. The protein was then dialyzed against 25 mM Hepes (pH 7.4), 150 mM NaCl, and 5% glycerol; concentrated to 1 mg/mL using a spin concentrator; split into aliquots; flash-frozen in liquid N_2; and stored at −80 °C.

SEC-MALS

For SEC-MALS analysis, we used a miniDAWN TREOS multi-angle light scattering detector, with three angle detectors (43.6°, 90°, and 136.4°) and a 658.9-nm laser beam (Wyatt Technology, Santa Barbara, CA) with a Wyatt QELS dynamic light scattering module for determination of hydrodynamic radius and an Optilab T-rEX refractometer (Wyatt Technology) set in-line with size exclusion chromatography analytical column Superdex 200 Increase 10/300 GL (GE, Life Science, Marlborough, MA) to which 150 μL of 1.17 mg/mL SARM1 and 75 μL of 8 mg/mL SAM$^{1-2}$ were injected. Experiments were performed using an AKTA Pure M25 system with a UV-900 detector (GE) adapted for analytical runs. All experiments were performed at room temperature (25 °C) at 0.8 mL/min, with running buffer of 25 mM Hepes (pH 7.4), 150 mM NaCl, and 0.5 mM DTT. Data collection and SEC-MALS analysis were performed with ASTRA 6.1 software (Wyatt Technology). The refractive index of the solvent was defined as 1.331, and the viscosity was defined as 0.8945 cP (common parameters for PBS buffer at 658.9 nm). dn/dc (refractive index increment) value for all samples was defined as 0.185 mL/g (a standard value for proteins).

Electron microscopy imaging and processing

To remove protein aggregates prior to electron microscopy analysis, isolated SARM1 was subjected to ultracentrifugation for 16 h at 4 °C in a 10%–25% glycerol gradient with a 0–0.1% glutaraldehyde gradient using a SW41Ti rotor, as we have previously performed [37]. For imaging, the sample was applied to carbon-coated copper grids (400 mesh) and washed twice in deionized water before stained with 1% uranyl-acetate (Electron Microscopy Sciences, USA). The samples were imaged with a JEOL 2100f electron microscope operating at 200 kV (JEOL, Japan). The images were recorded with a 4k pixel CCD camera (TVIPS, Germany) at a pixel size of 1.75 Å. The images were processed in the SCIPION software framework [38]. The CTF was estimated with CTFFIND4 [39], and the phases were flipped for further processing. A total of 13,463 particles were picked in SCIPION and then classified in 2D with Relion 2.1 [40].

Crystallization and data collection

Both native (final conc. 16 mg/mL) and SeMet (final conc. 14 mg/mL) SAM$^{1-2}$ were screened for crystal growth conditions with the commercial crystallization screens PEGRx HT, PEG/Ion HT, and Crystal Screen HT (Hampton Research, Aliso Viejo, CA, USA). This was accomplished at 20 °C in 96-well hanging-drop clear polystyrene microplates (TTP LabTech) using the mosquito robot for crystallography (TTP LabTech) as in Ref. [41]. A 1:1 sample/reservoir ratio was used with a drop size of 0.5 μL.

A relatively high number of hits were received, and most of them were refined in 24-well hanging-drop vapor diffusion plates by varying the pH value and concentration/molecular mass of the precipitant. Diffraction data were measured at 100K on beamlines ID14.1 and ID14.2 [42] at Berliner Elektronenspeicherring-Gesellschaft für Synchrotronstrahlung (BESSY) II (Berlin, Germany) and on the ID30-B and ID29 beamlines at the European Synchrotron Radiation Facility (ESRF) [43]. The best diffracting native crystals were obtained from 2% Tacsimate (pH 7), 5% v/v 2-propanol, 0.1 M imidazole (pH 7), and 8% *w*/v polyethylene glycol 3350 that was cryoprotected prior to flash-cooling in liquid nitrogen by gradual addition of 15% glycerol to the mother liquor. SeMet crystals with the strongest anomalous signal were received from 3% Tacsimate (pH 6) and 7% polyethylene glycol 3350 that were cryo-protectant in 4% Tacsimate (pH 6), 8% polyethylene glycol 3350, and 26% glycerol.

Structure determination and refinement

Native and anomalous data were processed with XDSapp and XDS [44,45]. The SAM^{1-2} crystal structure was solved in the tetragonal space group $P4_3$ with unit cell parameters $a = b = 252.2$, $c = 49.8$ Å by SeMet peak SAD method using the Crank2 experimental phasing pipeline [31] installed on the CCP4 cloud server [46]. Positions of the anomalous scatterers were located using SHELXD [47]. Additional CCP4 [48] programs were used in the pipeline including PARROT [49], BUCCANEER [50], and REFMAC5 [51]. The Crank2 pipeline has built a near-complete model containing two SAM^{1-2} octamers and refined it to Rfree of 0.318. Further refinement was conducted against higher-resolution native data using REFMAC5. Sixteen-fold NCS averaging was performed by DM [49] with density modification phases used in REFMAC5 refinement. The quality of the resulting combined maps was sufficient to build a solvent structure and some alternative conformations for residue side chains in COOT [52]. Structure validation was performed in the REFMAC5/Molprobity [53] script implemented in the CCP4i2 graphical interface [54].

The peak SeMet data were also collected for a second crystal form, which was originally indexed as $P4_222$ with $a = b = 90.4$, $c = 187.4$ Å; however, the structure could not be solved by experimental phasing or by molecular replacement to produce a full octameric model from the first crystal form. Data were reprocessed in P1, and molecular replacement with MOLREP [55] has positioned the SAM^{1-2} octamers in the triclinic unit cell. ZANUDA [56] has identified the true space group as $P2_12_12$ with $a = c = 90.4$, $b = 187.4$ Å, which is non-merohedrally twinned.

Resazurin cell viability assay

HEK293T cells were seeded onto lysine precoated 24-well plates (100,000 cells in each well) in final volume of 500 μL of DMEM (10% FBS) and incubated overnight in 37 °C under 5% CO_2. They were then transfected with different SARM1 constructs using the calcium phosphate-mediated transfection protocol [57], with addition of 25 μM Chloroquine (Sigma) right before the transfection. Six hours after transfection, the chloroquine-containing DMEM was replaced by fresh complete medium. After 24 h, the medium was removed and replaced with 0.03 mg/mL Resazurin sodium salt (Sigma) dissolved in Phenol Red free DMEM. All plates were than incubated for 1 h in 37 °C and measured using a SynergyHI (BioTek) plate reader at 560-nm excitation and 590-nm emission wavelengths. All fluorescent emission readings were averaged and normalized by subtracting the Resazurin background (measured in wells without cells) and then divided by the mean fluorescence emission from cells transfected by the empty vector (pCDNA3).

To visualize and record the effect of SARM1 constructs on cultured cells (Fig. 6B), HEK293T cells were transfected using TurboFect Transfection Reagent (Thermo). 75K cells were seeded on each well in 24-well plate 24 h before the transfection. One microgram of DNA from all constructs was diluted in 100 μL of serum-free DMEM. After dilution, 2 μL of transfection reagent was added to diluted DNA, vortexed, and incubated for 15 min in room temperature. After incubation, all 100 μL of reagent/DNA mix was added to appropriate well and incubated in 37 °C, 5% CO_2. Pictures were taken using JuLITM STAGE Real-Time Cell History Recorder (NanoEnTek Inc.) immediately after transfection and 24 h later.

Glutaraldehyde crosslinking assay

Purified WT and mutated SAM^{1-2} were diluted to a final concentration of 0.5 mg/mL in 25 mM Hepes (pH 7.5), 150 mM NaCl, and 1 mM DTT and then treated with 0.1% glutaraldehyde (Alfa Aesar) in 4 °C, and aliquots were taken from the reaction at 5 and 20 min and 1, 2, and 4 h. All samples were subsequently analyzed for oligomerization by SDS-PAGE.

Accession numbers

Coordinates and structure factors have been deposited in the Protein Data Bank with accession number 6QWV.

Acknowledgments

We thank the staff of beamlines ID30-B and ID29 of ESRF, and the staff of BESSY II BL14.1 and BL14.2. This work received funds from ISF (Israel Science Foundation) (Grant No. 1425/15 to Y.O.).

Received 25 April 2019;
Received in revised form 16 June 2019;
Accepted 25 June 2019

Keywords:
SARM1;
SAM domain;
cell death;
x-ray crystallography;
electron microscopy

Abbreviations used:

TRIF, TIR domain–containing adaptor inducing interferon-β; SARM1, sterile α and HEAT/armadillo motif-containing protein; TIR, Toll/interleukin-1 receptor; ML, mid-loop; EH, end-helix; SEC-MALS, size exclusion chromatography with multi-angle light scattering; SAD, single-wavelength anomalous dispersion; βME, β-mercaptoethanol.

References

[1] M. Carty, R. Goodbody, M. Schroder, J. Stack, P.N. Moynagh, A.G. Bowie, The human adaptor SARM negatively regulates adaptor protein TRIF-dependent toll-like receptor signaling, Nat. Immunol. 7 (2006) 1074–1081.

[2] P. Mukherjee, T.A. Woods, R.A. Moore, K.E. Peterson, Activation of the innate signaling molecule MAVS by bunyavirus infection upregulates the adaptor protein SARM1, leading to neuronal death, Immunity. 38 (2013) 705–716.

[3] Y.J. Hou, R. Banerjee, B. Thomas, C. Nathan, A. Garcia-Sastre, A. Ding, et al., SARM is required for neuronal injury and cytokine production in response to central nervous system viral infection, J. Immunol. 191 (2013) 875–883.

[4] Y. Kim, P. Zhou, L. Qian, J.Z. Chuang, J. Lee, C. Li, et al., MyD88-5 links mitochondria, microtubules, and JNK3 in neurons and regulates neuronal survival, J. Exp. Med. 204 (2007) 2063–2074.

[5] A. Waller, Experiments on the section of the glossopharyngeal and hypoglossal nerves of the frog, and observations of the alterations produced thereby in the structure of their primitive fibres, Philos. Trans. R. Soc. 140 (1850) 7.

[6] M.J. Geden, M. Deshmukh, Axon degeneration: context defines distinct pathways, Curr. Opin. Neurobiol. 39 (2016) 108–115.

[7] J.M. Osterloh, J. Yang, T.M. Rooney, A.N. Fox, R. Adalbert, E.H. Powell, et al., dSarm/Sarm1 is required for activation of an injury-induced axon death pathway, Science. 337 (2012) 481–484.

[8] J. Gerdts, D.W. Summers, Y. Sasaki, A. DiAntonio, J. Milbrandt, Sarm1-mediated axon degeneration requires both SAM and TIR interactions, J. Neurosci. 33 (2013) 13569–13580.

[9] D.R. Nanyes, S.E. Junco, A.B. Taylor, A.K. Robinson, N.L. Patterson, A. Shivarajpur, et al., Multiple polymer architectures of human polyhomeotic homolog 3 sterile alpha motif, Proteins. 82 (2014) 2823–2830.

[10] R. Goldner, A. Yaron, TIR axons apart: unpredicted NADase controls axonal degeneration, Neuron. 93 (2017) 1239–1241.

[11] P. Panneerselvam, L.P. Singh, B. Ho, J. Chen, J.L. Ding, Targeting of pro-apoptotic TLR adaptor SARM to mitochondria: definition of the critical region and residues in the signal sequence, Biochem. J. 442 (2012) 263–271.

[12] Z.Y. Zhao, X.J. Xie, W.H. Li, J. Liu, Z. Chen, B. Zhang, et al., A cell-permeant mimetic of NMN activates SARM1 to produce cyclic ADP-ribose and induce non-apoptotic cell death, iScience. 15 (2019) 452–466.

[13] K. Essuman, D.W. Summers, Y. Sasaki, X. Mao, A. DiAntonio, J. Milbrandt, The SARM1 toll/Interleukin-1 receptor domain possesses intrinsic NAD(+) cleavage activity that promotes pathological axonal degeneration, Neuron. 93 (2017) 1334–43 e5.

[14] K. Essuman, D.W. Summers, Y. Sasaki, X. Mao, A.K.Y. Yim, A. DiAntonio, et al., TIR domain proteins are an ancient family of NAD(+)-consuming enzymes, Curr. Biol. 28 (2018) 421–30 e4.

[15] S. Geisler, S.X. Huang, A. Strickland, R.A. Doan, D.W. Summers, X. Mao, et al., Gene therapy targeting SARM1 blocks pathological axon degeneration in mice, J. Exp. Med. 216 (2019) 294–303.

[16] Q. Yin, T.M. Fu, J. Li, H. Wu, Structural biology of innate immunity, Annu. Rev. Immunol. 33 (2015) 393–416.

[17] M.D. Sikowitz, L.E. Cooper, T.P. Begley, P.A. Kaminski, S.E. Ealick, Reversal of the substrate specificity of CMP *N*-glycosidase to dCMP, Biochemistry. 52 (2013) 4037–4047.

[18] J. Gerdts, E.J. Brace, Y. Sasaki, A. DiAntonio, J. Milbrandt, SARM1 activation triggers axon degeneration locally via NAD(+) destruction, Science. 348 (2015) 453–457.

[19] J. Gerdts, D.W. Summers, J. Milbrandt, A. DiAntonio, Axon self-destruction: new links among SARM1, MAPKs, and NAD+ metabolism, Neuron. 89 (2016) 449–460.

[20] F. Qiao, J.U. Bowie, The many faces of SAM, Sci. STKE 2005 (2005) re7.

[21] C.P. Ponting, SAM: a novel motif in yeast sterile and *Drosophila* polyhomeotic proteins, Protein science : a publication of the Protein Society. 4 (1995) 1928–1930.

[22] C.A. Kim, M. Gingery, R.M. Pilpa, J.U. Bowie, The SAM domain of polyhomeotic forms a helical polymer, Nat. Struct. Biol. 9 (2002) 453–457.

[23] C.A. Kim, M.L. Phillips, W. Kim, M. Gingery, H.H. Tran, M.A. Robinson, et al., Polymerization of the SAM domain of TEL in leukemogenesis and transcriptional repression, EMBO J. 20 (2001) 4173–4182.

[24] F. Qiao, H. Song, C.A. Kim, M.R. Sawaya, J.B. Hunter, M. Gingery, et al., Derepression by depolymerization; structural insights into the regulation of Yan by Mae, Cell. 118 (2004) 163–173.

[25] C.A. Kim, M.R. Sawaya, D. Cascio, W. Kim, J.U. Bowie, Structural organization of a sex-comb-on-midleg/polyhomeotic copolymer, J. Biol. Chem. 280 (2005) 27769–27775.

[26] M.K. Baron, T.M. Boeckers, B. Vaida, S. Faham, M. Gingery, M.R. Sawaya, et al., An architectural framework that may lie at the core of the postsynaptic density, Science. 311 (2006) 531–535.

[27] A.D. Meruelo, J.U. Bowie, Identifying polymer-forming SAM domains, Proteins. 74 (2009) 1–5.

[28] M.J. Knight, C. Leettola, M. Gingery, H. Li, J.U. Bowie, A human sterile alpha motif domain polymerizome, Protein science : a publication of the Protein Society. 20 (2011) 1697–1706.

[29] H.J. Lee, P.K. Hota, P. Chugha, H. Guo, H. Miao, L. Zhang, et al., NMR structure of a heterodimeric SAM:SAM complex: characterization and manipulation of EphA2 binding reveal new cellular functions of SHIP2, Structure. 20 (2012) 41–55.

[30] L. Zhang, M. Buck, Molecular simulations of a dynamic protein complex: role of salt-bridges and polar interactions in configurational transitions, Biophys. J. 105 (2013) 2412–2417.

[31] P. Skubak, D. Arac, M.W. Bowler, A.R. Correia, A. Hoelz, S. Larsen, et al., A new MR-SAD algorithm for the automatic building of protein models from low-resolution x-ray data and a poor starting model, IUCrJ. 5 (2018) 166–171.

[32] T.D. Mueller, J.L. Zhang, W. Sebald, A. Duschl, Structure, binding, and antagonists in the IL-4/IL-13 receptor system, Biochim. Biophys. Acta 1592 (2002) 237–250.

[33] E. Latz, T.S. Xiao, A. Stutz, Activation and regulation of the inflammasomes, Nat Rev Immunol. 13 (2013) 397–411.

[34] M. Carty, J. Kearney, K.A. Shanahan, E. Hams, R. Sugisawa, D. Connolly, et al., Cell survival and cytokine release after inflammasome activation is regulated by the toll-IL-1R protein SARM, Immunity. 50 (2019) 1412–1424 (e6).

[35] R. Barak, Y. Opatowsky, Expression, derivatization, crystallization and experimental phasing of an extracellular segment of the human Robo1 receptor, Acta Crystallogr. Sect. F: Struct. Biol. Cryst. Commun. 69 (2013) 771–775.

[36] J. Guez-Haddad, M. Sporny, Y. Sasson, L. Gevorkyan-Airapetov, N. Lahav-Mankovski, D. Margulies, et al., The neuronal migration factor srGAP2 achieves specificity in ligand binding through a two-component molecular mechanism, Structure. 23 (2015) 1989–2000.

[37] R. Barak, R. Lahmi, L. Gevorkyan-Airapetov, E. Levy, A. Tzur, Y. Opatowsky, Crystal structure of the extracellular juxtamembrane region of Robo1, J. Struct. Biol. 186 (2014) 283–291.

[38] J.M. de la Rosa-Trevin, A. Quintana, L. Del Cano, A. Zaldivar, I. Foche, J. Gutierrez, et al., Scipion: a software framework toward integration, reproducibility and validation in 3D electron microscopy, J. Struct. Biol. 195 (2016) 93–99.

[39] A. Rohou, N. Grigorieff, CTFFIND4: fast and accurate defocus estimation from electron micrographs, J. Struct. Biol. 192 (2015) 216–221.

[40] S.H. Scheres, RELION: implementation of a Bayesian approach to cryo-EM structure determination, J. Struct. Biol. 180 (2012) 519–530.

[41] M. Sporny, J. Guez-Haddad, D.G. Waterman, M.N. Isupov, Y. Opatowsky, Molecular symmetry-constrained systematic search approach to structure solution of the coiled-coil SRGAP2 F-BARx domain, Acta crystallographica Section D, Structural biology. 72 (2016) 1241–1253.

[42] U. Mueller, N. Darowski, M.R. Fuchs, R. Förster, M. Hellmig, K.S. Paithankar, et al., Facilities for macromolecular crystallography at the Helmholtz–Zentrum Berlin, J. Synchrotron Radiat. 19 (2012) 442–449.

[43] D. Nurizzo, T. Mairs, M. Guijarro, V. Rey, J. Meyer, P. Fajardo, et al., The ID23-1 structural biology beamline at the ESRF, J. Synchrotron Radiat. 13 (2006) 227–238.

[44] Krug MW, M. S; Heinemann, U; and Mueller, U. . XDSAPP: a graphical user interface for the convenient processing of diffraction data using XDS. J. Appl. Crystallogr. 2012;45:5.

[45] W. Kabsch, Xds, Acta Cryst D. 66 (2010) 125–132.

[46] E. Krissinel, V. Uski, A. Lebedev, M. Winn, C. Ballard, Distributed computing for macromolecular crystallography, Acta crystallographica Section D, Structural biology. 74 (2018) 143–151.

[47] T.R. Schneider, G.M. Sheldrick, Substructure solution with SHELXD, Acta Crystallogr D Biol Crystallogr. 58 (2002) 1772–1779.

[48] M.D. Winn, C.C. Ballard, K.D. Cowtan, E.J. Dodson, P. Emsley, P.R. Evans, et al., Overview of the CCP4 suite and current developments, Acta Cryst D. 67 (2011) 235–242.

[49] K. Cowtan, Recent developments in classical density modification, Acta Cryst D. 66 (2010) 470–478.

[50] K. Cowtan, The Buccaneer software for automated model building. 1. Tracing protein chains, Acta Cryst D. 62 (2006) 1002–1011.

[51] G.N. Murshudov, P. Skubak, A.A. Lebedev, N.S. Pannu, R.A. Steiner, R.A. Nicholls, et al., REFMAC5 for the refinement of macromolecular crystal structures, Acta Crystallogr D Biol Crystallogr. 67 (2011) 355–367.

[52] P. Emsley, B. Lohkamp, W.G. Scott, K. Cowtan, Features and development of Coot, Acta Cryst D. 66 (2010) 486–501.

[53] C.J. Williams, J.J. Headd, N.W. Moriarty, M.G. Prisant, L.L. Videau, L.N. Deis, et al., MolProbity: more and better reference data for improved all-atom structure validation, Protein science: a publication of the Protein Society. 27 (2018) 293–315.

[54] L. Potterton, J. Agirre, C. Ballard, K. Cowtan, E. Dodson, P.R. Evans, et al., CCP4i2: the new graphical user interface to the CCP4 program suite, Acta crystallographica Section D, Structural biology. 74 (2018) 68–84.

[55] A. Vagin, A. Teplyakov, Molecular replacement with MOLREP, Acta Cryst D. 66 (2010) 22–25.

[56] A.A. Lebedev, M.N. Isupov, Space-group and origin ambiguity in macromolecular structures with pseudo-symmetry and its treatment with the program Zanuda, Acta Crystallogr D Biol Crystallogr. 70 (2014) 2430–2443.

[57] Kingston RE, Chen CA, Rose JK, Calcium phosphate transfection. 2003;Curr Protoc Mol Biol Chapter 9:Unit 9.1.

[58] P.A. Karplus, K. Diederichs, Linking crystallographic model and data quality, Science 336 (2012) 1030–1033.

[59] A.A. Vaguine, J. Richelle, S.J. Wodak, SFCHECK: A unified set of procedures for evaluating the quality of macromolecular structure-factor data and their agreement with the atomic model, Acta Crystallogr. D Biol. Crystallogr. 55 (1999) 191–205.